Properties of Hermean plasma belt: numerical simulations and comparison with MESSENGER data

David Herčík[1,2,3], Pavel M. Trávníček[4,2,3], Štěpán Štverák[3,2], and Petr Hellinger[2,3]

Abstract.
Using a global hybrid model and test particle simulations we present a detailed analysis of the Hermean plasma belt structure. We investigate characteristic properties of quasi-trapped particle population characteristics and its behavior under different orientations of the interplanetary magnetic field. The plasma belt region is constantly supplied with solar wind protons via magnetospheric flanks and tail current sheet region. Protons inside the plasma belt region are quasi-trapped in the magnetic field of Mercury and perform westward drift along the planet. This region is well separated by a magnetic shell and has higher average temperatures and lower bulk proton current densities than the surrounding area. On the dayside the population exhibits loss cone distribution function matching the theoretical loss cone angle. The simulation results are in a good agreement with in situ observations of MESSENGER's MAG and FIPS instruments.

1. Introduction

The Earth's magnetospheric structure is quite well known thanks to many magnetospheric missions. One of the magnetospheric features is the ring current, i.e., an electric current formed by magnetically trapped particles drifting around Earth and forming a toroidally shaped structure. The structure is located at the magnetic equatorial plane in the distances $\approx 2-9R_E$ (R_E - Earth's radii) [*Daglis et al.*, 1999]. The major constituent of the terrestrial ring current during quiet magnetospheric times is the solar wind ion population. During storm times with enhanced geomagnetic activity, the ionospheric particles, mainly O^+, are out-flowing and contributing significantly to the ring current density [*Daglis*, 1997].

Before the MESSENGER's [*Slavin et al.*, 2007] insertion into the orbit around Mercury, it was not clear, whether Mercury possesses such a similar plasma belt feature. Mercury, as indicated by Mariner 10 [*Dunne and Burgess*, 1978] and confirmed by the MESSENGER magnetometer measurements, has its own intrinsic magnetic field. The dynamo is producing a much smaller magnetic moment (≈ 190 $\mathrm{nT}R_M^3$[*Anderson et al.*, 2011]) than in case of Earth. However, it is still sufficient to form a magnetospheric structure similar to the terrestrial one [*Travnicek et al.*, 2010, e.g.], but significantly smaller. The whole potential plasma belt region has been expected to be below 1 Hermean radii (R_M) [*Russell et al.*, 1988]. Recently, numerical simulations [*Travnicek et al.*, 2010; *Yagi et al.*, 2010] as well as data from MESSENGER [*Schriver et al.*, 2011] shown formation of the ring current with the quasi-trapped population to be possible.

Mercury, unlike Earth, lacks significant ionosphere. Hermean neutral exosphere has been observed by Mariner 10 [*Dunne and Burgess*, 1978] and by ground based observations [*Morgan and Killen*, 1997]. MESSENGER's [*Solomon et al.*, 2001] measurements revealed that sodium represents significant constituent of Mercurys exosphere and sodium pick-up ions have been observed in the inner magnetosphere as well as in Mercury's magnetosheath [*Sarantos et al.*, 2009]. The sodium is populated from the Hermean surface mainly by the photon stimulated desorption (PSD) and solar wind sputtering (SWS) [*Leblanc and Johnson*, 2003]. The PSD plays significant role on the dayside releasing rather low energetic particles. SWS acts mainly near the auroral zones, induced by solar wind particles hitting the planetary surface. As indicated by numerical simulations of *Paral et al.* [2010], Na^+ ions are formed mainly by the photoionization of the exosphere neutrals at Mercury's dayside. They are mostly confined between the surface and the magnetopause, they travel westward towards the nightside and extend into magnetospheric tail, as shows also by *Delcourt et al.* [2003]. The pick-up ions contribute to the ring current population, however, we should stress out that the main source of the ring current is likely carried by the solar wind particles entering the inner magnetosphere.

In the case of Earth, the inner magnetosphere is supplied by the ionospheric and solar wind plasma via various mechanisms and regions [*Moore et al.*, 2005]. Numerical simulations of the test particles entries to the inner magnetosphere using the topology of the magnetic field calculated by MHD code have been carried out in order to study the mechanism transporting these particles from the solar wind into the inner magnetosphere [*Richard et al.*, 1994; *Walker et al.*, 1995]. The results indicate that solar wind protons might enter the magnetosphere either through the cusp regions or in the magnetospheric flanks. A solar wind particle that enters cusp region moves along the magnetospheric field line and drifts along the planet contributing to the magnetospheric plasma. These particles can form also the low latitude boundary layer (LLBL) via high-latitude reconnection as proposed by *Song and Russell* [1992]. This mechanism would explain the LLBL layered mixture composition of magnetospheric and solar wind particles. LLBL was originally observed at the tail region, but similar boundary layer with magnetosheath-like plasma is found also at high latitudes in the dayside magnetosphere as well as in the tail plasma mantle [*Sckopke et al.*, 1981].

In case of Mercury, the dayside LLBL is probably merged with the ring current region as the magnetopause stand off

[1]Institute for Geophysics and Extraterrestrial Physics, Technical University, Braunschweig, DE
[2]Astronomical Institute, The Czech Academy of Sciences, Prague, CZ
[3]Institute of Atmospheric Physics, The Czech Academy of Sciences, Prague, CZ
[4]Space Sciences Laboratory, University California Berkeley, USA

0148-0227/16/2015JA021938$9.00

distance is estimated to be 1 to 2 R_M from the planetary center [*Goldstein et al.*, 1981] depending on the solar wind pressure. The magnetopause boundary layer (high and low latitude at dayside) will contribute to the ring current plasma.

Another source of the ring current region is the solar wind incoming from the magnetospheric flanks and the tail current sheet. *Ashour-Abdalla et al.* [1998] carried out an analysis of ion sources of one particular distribution function observed by Geotail in the near-Earth plasma sheet. The results, based on a single particle tracing via the MHD simulated fields, show the far tail magnetospheric flanks and the plasma mantle as the main sources for the ions observed. These regions are also probable sources of magnetospheric ions in case of Mercury as will be indicated here below.

The paper is organized as follows. In section 2 we introduce the simulation model and data used for the analysis. In section 3 an overview of a proton flux to the planetary surface and its comparison for six simulation cases is given. In section 4 an analysis of the plasma belt structure in all the presented cases is provided. In section 5 we attempt to uncover possible ion sources for the plasma belt. Afterwards, a more detailed analysis is limited to one selected simulation. In section 6, energization of protons from the solar wind to the plasma belt is discussed. In section 7 we focus on quasi trapped particles within the plasma belt, their properties and behavior within the selected simulation case. In section 8 we compare in situ data acquired by the MESSENGER mission with matching simulation data. A discussion on selected features analyzed within the study as well as the results validity is presented in section 9.

2. Simulations

Data used for the analysis results from hybrid simulations of the solar wind interaction with the Hermean magnetosphere. Previous models and results were published in *Travnicek et al.* [2007] and described more in detail in *Travnicek et al.* [2010]. An updated simulation model with new runs was presented in *Herčík et al.* [2013]. The same datasets analyzed in *Herčík et al.* [2013] are used in this paper. The new improved simulations reflect in situ observations of the MESSENGER spacecraft, in particular the dipole magnetic field strength and its offset towards the north pole. Furthermore, the spatial resolution of the models was refined. The simulation box coordinates have origin in the center of Mercury with $+x$-direction along the solar wind flow, $+z$-direction along the magnetic dipole axis and $+y$-direction completing the right-hand coordinate system.

A downscaled model of Mercury is used with a magnetic moment $M = 100,000 B_{\rm sw} d_{p\rm sw}^3 4\pi/\mu_0$, where $B_{\rm sw}$ is the magnitude of the solar wind magnetic field, $d_{p\rm sw} = c/\omega_{pp\rm sw}$ is the proton inertial length in the solar wind, c is the speed of light, $\omega_{pp\rm sw}$ is the solar wind proton plasma frequency. The $d_{p\rm sw}$ is equivalent to the proton Larmor radius with Alfvén speed $d_{p\rm sw} \equiv v_{A\rm sw}/\omega_{gp\rm sw}$, where $\omega_{gp\rm sw}$ is the proton gyrofrequency in the solar wind. The downscaling preserves the stand-off magnetopause distance $R_{\rm mp}$ predicted from the pressure balance between the solar wind ram pressure $P_{\rm ram,sw}$ and the magnetospheric pressure: $R_{\rm mp} = [B_{\rm eq}^2/(2\mu_0 P_{\rm ram,sw})]^{1/6} R_M$, where $B_{\rm eq}$ is the magnetic field at the equator of the planet, which before downscaling corresponds to 195 nT. Following recent observations of MESSENGER [*Anderson et al.*, 2011], the dipolar magnetic field is shifted towards the north pole by 0.2 R_M. The scaling factor used in the simulations is 1.9, i.e., the simulated planet is 1.9 times smaller than it should be, taking the real conditions into account. Particular parameters of the model are presented in Table 1.

In the presented paper we analyze data from six simulation runs with the same initial conditions except the interplanetary magnetic field (IMF) orientation. These cases have been selected in order to be able to compare the influence of the change of the external conditions to the plasma belt structure. The six cases are denominated according to the IMF orientation as follows: **EIMF-P** means magnetic field parallel to the equatorial plane with planetward (-P) component. **EIMF-S** means magnetic field parallel to the equatorial plane with sunward component (-S). **SIMF-P** (**SIMF-S**) denominates southward IMF with planetward (sunward) component respectively and **NIMF-P** (**NIMF-S**) means northward IMF with planetward (sunward) component respectively. The overview of the simulation cases is given in Table 2.

Table 1. Simulation parameters

NIMF-P	
Number of cells $N_x \times N_y \times N_z$	$940 \times 400 \times 400$
Spatial resolution Δx [$d_{p\rm sw}$]	0.4
Spatial resolution $\Delta y = \Delta z$ [$d_{p\rm sw}$]	1.0
Size of the system $L_x = N_x \Delta x$ [$d_{p\rm sw}$]	376
Size of the system $L_y = L_z = N_y \Delta y$ [$d_{p\rm sw}$]	400
Hermean radius R_M [$d_{p\rm sw}$]	21.727
Temporal resolution (time step) Δt [$\omega_{gp\rm sw}^{-1}$]	0.02
Time sub-stepping for fields Δt_B [$\omega_{gp\rm sw}^{-1}$]	0.002
Duration of simulation [$\omega_{gp\rm sw}^{-1}$]	80
Number of macro-particles per cell	70
Total number of macro-particles	$\sim 10.5\times10^9$
Solar wind velocity $v_{p\rm sw}$ [$v_{A\rm sw}$]	4.0
Orientation of IMF in (X, Z) plane	$+20°$
Strength of IMF [nT]	20
Hermean magnetic moment M [nTR_M^3]	195*

$n_{p\rm sw}$, $B_{\rm sw}$, $v_{A\rm sw}$, $d_{p\rm sw}$, $\omega_{gp\rm sw} = 1$ (in simulation units)
* 1/5 R_M offset towards north

The simulation setup corresponds to the following solar wind conditions: the ambient magnetic field in the solar wind $B_{\rm sw} = 20$ nT, the proton inertial length in the solar wind $d_{p\rm sw}$ corresponds to $\sim$ 369 km. Proton solar wind density is considered to be $n_{p\rm sw} = 15$ cm^{-3} and the Alfvén velocity in the solar wind $v_{A\rm sw}$ is therefore approximately 112500 m/s. The proton plasma beta, ratio of the thermal and magnetic pressure, in the solar wind is set to $\beta = 0.5$. The proton current density in simulations is measured in units of unitary proton current density, i.e., the current density carried by protons of solar wind density ($n_{p\rm sw}$) moving with the proton Alfvén velocity ($v_{A\rm sw}$). The proton temperature in the simulations is measured in units of $B_{\rm sw}^2/(n_{p\rm sw}\mu_0)$.

3. Proton influx to the Mercury's surface

At Earth the plasma belt is connected to the planet by footprints of magnetic field lines, within which the plasma is confined, forming auroral ovals. At these regions particles from the plasma belt precipitate into the Earth's ionosphere.

First we compare the fluxes of particles onto the Hermean surface for the six simulated cases. Figure 1 shows proton fluxes accumulated during ten simulation time iterations, i.e., over a period of 0.2 $\omega_{gp\rm sw}^{-1}$. The fluxes are mapped as a function of longitude and latitude. Zero degree (0°) longitude corresponds to the midnight meridian and 180° corresponds to the sub-solar (noon) meridian. Longitudes $< 180°$ are at the dawn region and longitudes $> 180°$ are at dusk region. Zero degree 0° latitude is at geographic equator, $-90°$ denotes the south pole and $+90°$ the north pole. Red square indicates estimated southern and red circle northern cusp location.

Panels a and b show data from equatorial simulation case for the planetward (EIMF-P) and the sunward (EIMF-S) IMF orientation, respectively. We can see the tilt in the cusp positions towards dawn for northern cusp and towards dusk for southern cusp. This effect is known from Earth observations and is caused by the B_y component (east-west) of the IMF. Not only the position of cusps is rotated in that

Table 2. Orientation of IMF for all six studied simulation cases. IMF ϕ is the angle between the solar wind flow ($+\mathcal{X}$) direction and the IMF vector in the noon-midnight ($\mathcal{XZ}$) meridian plane. IMF θ is the angle between the solar wind flow ($+\mathcal{X}$) direction and the IMF vector in the equatorial ($\mathcal{XY}$) plane.

	EIMF-P	**SIMF-P**	**NIMF-P**	**EIMF-S**	**NIMF-S**	**SIMF-S**
	Planetward IMF			Sunward IMF		
IMF ϕ [°]	0	-20	+20	0	+160	-160
IMF θ [°]	-45	0	0	135	0	0

case, but all the magnetospheric features are turned along the subsolar line, current sheet is not aligned with equatorial plane, but is tilted, as well as the magnetospheric lobes. The rotation of the whole magnetosphere is present also in the simulation dataset (not shown here). The origin of the magnetospheric tilt is in the magnetic curvature force [*Hultqvist et al.*, 1996]. When IMF $B_y < 0$ (directed duskward) and a reconnection at the dayside takes place, pair of L-shaped open field lines are formed. The curvature magnetic force acts on the fluxtube connected to the northern cusp in such manner that it is dragged towards dawn. On the contrary the fluxtube connected to southern cusp is dragged towards dusk. This affects the whole magnetosphere that is then tilted anti-clockward, when looking in the planetward direction from the Sun. The opposite IMF B_y component has also the opposite effect.

Middle panels of Figure 1 show the precipitation of proton flux for southward IMF with the planetward component (SIMF-P, panel c) and the sunward component (SIMF-S, panel d). Bottom panels show situation for northward IMF with the planetward component (NIMF-P, panel e) and the sunward component (NIMF-S, panel f).

Comparing all the panels, we can conclude on several features. The first apparent feature in all the cases is the shift towards north, the fluxes are not symmetric across the geographic equator. This shift reflects the shift in the dipole field set in the initialization based on MESSENGER observations.

Another effect of the shift in the Mercury's dipole field is the amount of protons hitting each hemisphere. Due to the dipole shift, the magnetic field just above the surface in the northern hemisphere is stronger than in the southern hemisphere, resulting in a narrower cusp region in the north. Therefore, less particles precipitate in the northern hemisphere than to the southern due to the stronger mirror force. This can be seen in all the plots. Table 3 shows the percentage of the flux colliding with the southern hemisphere. In all the cases, the flux to the southern hemisphere represents more than a half of the total flux. Hereby, the total flux means all the particles impacting on the surface of the planet. In case of the sunward IMF orientation, almost all ($\approx$ 90%) of the particles hit the southern hemisphere. The cause for such behavior is likely a combined effect of the shift in magnetic dipole and the location of reconnection of the IMF field lines with the magnetospheric field lines.

Table 3. Particle flux percentage colliding on the southern hemisphere with respect to the total flux, where total flux means all particles impacting on the surface of the planet.

Case	**% of total flux**
EIMF-P	61
SIMF-P	54
NIMF-P	77
EIMF-S	88
SIMF-S	90
NIMF-S	93

For the planetward IMF the reconnection appears predominantly in the northern tail lobe and in southern part of the dayside magnetosphere, resulting in the field lines that have parts coming from the solar wind region connected to northern cusp. The parts of IMF field lines that extend behind the planet are connected to the southern cusp. Due to the reconnection asymmetry and the magnetosheath plasma flow, more solar wind plasma has access to the northern cusp region, in case the magnetic field dipole is located in the center of the planet. At Mercury, the planetary magnetic dipole is shifted towards the north pole, which results in a weaker mirror force in the southern cusp region. These two effects, the reconnection and dipole shift, act one against each other on opposite hemispheres, therefore comparable proton fluxes can be found on both hemispheres.

On the contrary, in case of the sunward IMF, the reconnection connects IMF field line part from the solar wind region to the southern cusp and the tail IMF field line part to the northern cusp. This results in a higher proton flux to the southern hemisphere, which is further enhanced by the Hermean magnetic dipole shift. Hence the ratio of flux to southern hemisphere can be around 90% as illustrate computed values in Table 3.

All the cases exhibit similar pattern, where on the nightside (near 0° or 360° longitude) the precipitation is at lower latitudes, while on the dayside (near 180° longitude) protons get closer the cusps at higher latitudes.

We can trace another effect of the reconnection by comparing panel c representing the SIMF-P case and panel e representing the NIMF-P case in Figure 1. In case of northward IMF (NIMF-P), the precipitated proton signatures at the dayside (around 180° longitude) are spread towards higher latitudes with more flux on the poleward sides of the cusps region (both in north and south hemispheres). This is the effect of the reconnection, which in case of northward IMF takes place in the tail region and protons then travel towards planet predominantly along the field lines connected poleward of the cusp. For SIMF-P (panel c), the reconnection takes place on the dayside and therefore the precipitation of protons is higher equatorward from the cusps. Such behavior is known from the Earth observations as well [*Hultqvist et al.*, 1996].

4. Plasma belt structure

The plasma belt region can be identified in the simulated data as the region around the planet with the increased proton density and with the enhanced plasma temperature. The plasma belt is formed in all the simulation cases that have been studied, however, its particular shape strongly depends on the IMF orientation. The dayside region might be suppressed by the small stand-off distance in case of the southward IMF. The main difference in the global plasma belt structure between the sunward and the planetward IMF orientations seems to be in opposite shift in the current sheet, that also corresponds to shift of the nightside plasma belt. For the sunward IMF, the current sheet in tail and also the nightside plasma belt is shifted southwards and for planetward IMF northwards.

The difference between northward and southward IMF cases is even more pronounced. The most visible difference is the aforementioned dayside part, but also on the nightside, the plasma belt structure is different in shape in equatorial as well as in meridian plane. Therefore we will limit

our detailed analysis to two cases for the northward (NIMF-P) and the southward IMF (SIMF-P) with the planetward component.

The situation for the NIMF-P case is demonstrated in Figure 2 that shows in simulation units the proton number density (panels a, d, and g), proton current density (panels b, e, and h), and proton temperature (panels c, f, and i) in the noon-midnight meridian (top panels a–c), magnetic equatorial (middle panels d–f), and dawn-dusk meridian plane (bottom panels g–i). The magnetic equator plane is here defined as a plane parallel to the equatorial plane, but shifted by 0.2 R_M towards the north, which corresponds to the shift of the Hermean magnetic dipole.

The plasma belt is visible around the whole planet on the density plots (a, d). On the dayside, the distinction between the plasma belt and the magnetopause boundary layer is not possible. On the nightside the plasma belt extends to $\sim$2 R_M. The black dashed line on panels d, e, and f indicates computed center of the plasma belt region and solid lines indicate its inner and outer boundaries. For the estimation of the boundaries, arbitrary thresholds have been used. For the inner boundary minimum density of 0.05 n_{sw} has been used as a threshold. For the outer boundary, plasma with temperatures higher than 5 in simulation units was assumed to be within the plasma belt region. The center of the plasma belt region is arbitrarily defined as the half of the radial distance from the aforementioned inner and outer boundary of the plasma belt in the magnetic equatorial plane. The width of the plasma belt varies from about 0.5 R_M ahead of the planet up to 1 R_M behind. The current density (b, e, h) as well as the temperature data (c, f, i) show two distinct regions on the nightside with lower proton current density and higher temperature near the planet and higher proton current density and lower temperature further in the tail.

Top panels show positions of six points arbitrary selected for a future reference and analysis. All the points lay in the noon-midnight meridian plane. Points N1, N1A, and N1B lay on the same magnetic field line NFL01 displayed by a black solid line going through these three points. Point N1 is 1.7 R_M from the planetary center at the lowest magnetic field intensity location along the dedicated field line. Points N1A and N1B at the beginning and end, respectively, of the fieldline NFL01 near the planetary surface ($\approx 5d_{\rm psw}$). Point N2 is 2.3 R_M from the planetary center at the field line NFL02 (again showed by a solid black line) which approximately separates the two regions mentioned above, i.e., the regions of lower and higher proton current density. Point N3 is 3.1 R_M from the planetary center. Point N4 is on the dayside field line NFL04 1.4 R_M ahead of the planetary center. Points NM1 and NM2 are placed in the dawn/dusk regions of the plasma belt center at a mean central distance of $\sim$1.4 R_M from the planetary center.

Figure 3 illustrates the similar situation as Figure 2, but this time for the southward IMF (SIMF-P) simulation case. It again shows the proton particle density (panels a, d, and g), proton current density (panels b, e, and h), and proton temperature (panels c, f, and i) in the noon-midnight meridian (top panels a–c), magnetic equatorial (middle panels d–f), and dawn-dusk meridian plane (bottom panels g–i).

Clearly, the dayside magnetosphere restricts the plasma belt significantly in this case. However, even here, the dayside magnetosphere exhibits higher proton temperatures, which is an indication for undergoing heating process and therefore a signature of quasi-trapped particles being present. The nightside plasma belt has a similar region of heated plasma and low proton current density as the NIMF-P case. Here the field line SFL02, that approximates the boundary of heated region, extends to $\approx 2.2R_M$ behind the planet (in $\mathcal{X}$ direction). The point S2 is at the minimum magnetic field position along field line SFL02 being $2.3R_M$ far from the planetary center. Comparing to the NIMF-P case, we can see, that the extension of the heated region in $\mathcal{X}$ direction is similar for both simulations (SIMF-P and NIMF-P). In the north-south direction however, the thickness is smaller for the SIMF-P case, as the field lines are squeezed together by the higher total pressure in the magnetospheric lobes. This also affects the region further towards the tail current sheet with higher current density. We can see, that the region is squeezed between the lobes forming narrow current fluxes around the heated protons region. We have selected points for a future analysis also in this simulation case. Points S1A, S1, and S1B lie on the same field line SFL01, being at its start, middle (minimum **B** field), and its end respectively. Point S1 is 1.7 R_M from the planetary center. Point S3 is in the plasma sheet further in the tail (approx. $2.8R_M$ from the planetary center) and S4 is in the dayside magnetosphere $\sim 0.2R_M$ ahead of the planetary surface.

We have calculated a velocity distribution function (VDF) at each of the points mentioned above in order to compare the different regions in terms of plasma composition. Trapped or quasi-trapped particle populations exhibit a loss cone distribution, where particles with velocity vector quasi-parallel to the magnetic field line can escape towards the planet. On the contrary, particles with higher perpendicular velocity component become trapped in the magnetic mirror and can undergo an acceleration process.

Figure 4 shows a comparison of velocity distribution functions at four points (S1,S1A,S1B,S4) for the simulation SIMF-P indicated in Figure 3 and four points (N1,N1A,N1B,N4) from the simulation NIMF-P indicated in Figure 2. The VDF is calculated as a histogram from the simulation data using the velocities of particles acquired within a sphere with radius of 3 proton inertial lengths ($d_{\rm psw} = c/\omega_{pp\rm sw}$) with the center at the point of interest. The distribution is normalized to density and averaged over the gyration phase angle (ϕ) as $\tilde{f}(v_\parallel, v_\perp) = 1/v_\perp \sum_\phi f(v_\parallel, v_\perp, \phi)$. To avoid numerical problems around $v_\perp = 0$, values of the distribution function are set to 0 for $v_\perp < 0.01$. The computed VDF is furthermore mirrored along the $v_\parallel$ axis for visualization purposes. Velocities are displayed in the units of Alfvén velocity in the solar wind $v_{A\rm sw}$.

Panel a shows VDF at the point S1. It shows a wide spread in velocities indicating high temperature. No loss-cone in this case can be identified. For comparison, panel d shows VDF at the point S4, that is in the field line center location, but on the dayside of the planet. There is a strong difference in the particle distribution. Here the distribution, even if very sparse, exhibits a loss-cone shape that indicates trapped particles in the Hermean magnetic field. The reason for this difference, when comparing day and nightside, is likely in the sources of the particles. Meanwhile the nightside plasma belt is being constantly supplied with the solar wind particles coming from the current sheet and magnetospheric flanks, the dayside plasma belt has the main source of particles in the drift around the planet. Therefore here, the plasma population consists mainly of the trapped or quasi-trapped particles.

Comparing the distribution functions from the two field line ends (S1A,S1B), we see only partial loss-cones. At panel b, that corresponds to point S1A (the beginning of the respective field line), the particles having high positive parallel component of the velocity are missing in the population. Hence, here the particles coming from the surface are missing, while particles traveling towards the surface are present. At panel c (point S1B - end of field line) the situation is reversed. The population lacks quasi-parallel traveling particles with a high negative parallel component. It means that again some amount of particles hit the surface and are not mirroring back.

Similar VDFs are acquired at the point N1 (panel e), N1A (panel f), and N1B (panel g). Also here at the middle point (N1), the VDF shows a wide spread in energies. At the point N1A (field line beginning), there is a deficiency in particles traveling from the surface as well as in the point N1B at the end of the field line.

At the point S4, only a few particles can be found, but still the loss cone in the VDF can be identified. More visible is the VDF shape acquired at the point N4 on the dayside magnetosphere. As panel h shows, there is a loss-cone distribution with quite a broad loss-cone. The situation is clearer on the pitch angle distribution function (PAD) displayed in Figure 5. The PAD for plasma at location N4 is sharp with lack of particles with pitch angles quasi-parallel with the ambient magnetic field. The loss-cone pitch angle can be estimated from Figure 5 at location N4 to be about $\alpha = 40^\circ$ to 50°. The expected theoretical value of the loss-cone pitch angle is given by

$$\alpha = \arcsin\left(\sqrt{\frac{B_{min}}{B_{max}}}\right), \quad (1)$$

where B_{min} and B_{max} are the minimum and maximum values of the magnetic field along the given magnetic field line. For the dayside field line NFL04, we have estimated the theoretical loss-cone angle to be $\alpha = 43^\circ$, which well corresponds to the observed PAD and VDF.

When looking into the PAD at the N1 location, it shows no loss-cone, however we expect trapped or quasi-trapped particles to be present here as well, due to high energies observed. The theoretical value would indicate loss-cone angle at the NFL01 to be around 25°. The reason for this discrepancy is probably the constant supply of newly incoming protons of the solar wind origin to this region.

The PADs confirm the results already indicated by the VDFs and described above, i.e., the loss-cone distribution and the magnetic mirror effect.

5. Sources of Mercury's plasma belt

The sources of the Earth's inner magnetosphere have been investigated by the test particle approach, e.g., by *Richard et al.* [1994]; *Walker et al.* [1995]. The results indicate that solar wind plasma can enter the inner magnetosphere either in the cusp region or at the magnetospheric flanks. We have investigated flowlines resulting from bulk properties of simulated protons rather than using test particles in order to see a general proton flow and to identify possible entry locations from the magnetosheath. In this part of the study we have focused on one simulation case only, in particular on the NIMF-P simulation run with northward IMF component.

The upper panels of Figure 6 show three examples of the flowlines backtracked from the points N1, N3, and NM2 (as indicated in Figure 2). The calculation is done by a fourth order Runge-Kutta method using bulk velocities from the simulation. The black line shows a flowline representing the solar wind protons coming towards the planet near the equatorial plane slightly at the dusk side of the planet ($\mathcal{Y} = -0.52R_M$). The flow is diverted at the magnetopause towards the dusk side and goes along the magnetopause boundary up to position at around $\mathcal{X} = 3.5R_M$ behind the planet center, where it enters the inner magnetosphere through the magnetospheric flank. The protons flow towards the central current sheet up to point 2 indicated in top panels of Figure 6. Here the flow is deflected again, probably within the main current sheet flow channel, this time towards the planet. Upon entering the plasma belt structure at point 3, the flow follows westward drift of the plasma belt protons up to the point NM2.

The middle and bottom panels in Figure 6 are discussed later in section 6.

The green solid line indicates another flowline, that was calculated backwards from point N3 in the plasma sheet behind the planet. The flow starts in the solar wind close to the sub-solar point. The bow shock crossing change the direction of the flow mainly northward. When the flow reaches magnetopause, the protons are carried away by the magnetopause currents that flow in the dayside magnetopause along the cusp in the eastward direction. This tail current system is consistent with the theoretical expectation taking into account the direction of the Hermean magnetic field close to cusp and in the lobes. Further on, the proton flow follows the magnetopause currents in the tail, going along the dawn-flank of the magnetosphere and entering the current sheet in the far tail (at $\mathcal{X} > 6R_M$). The flow is then deflected towards the planet and with increased velocity (not shown in the Figure) is transported to point N3 in the plasma sheet.

The last example of a flowline is shown by the red solid line. The beginning of the flow is similar to the green line, i.e., almost at the sub-solar point, slightly toward the dawn side ($\mathcal{Y} \sim 0.13R_M$). In the magnetosheath the protons flow towards the dawn side of the planet along the flank up to the point at around $\mathcal{X} = 2R_M$ behind the planet, where the flow enters the inner magnetosphere and further on the plasma belt itself. Within the plasma belt, the westward drift is visible for the red flowline example as well.

Shown examples as well as other studied flowlines indicate that the major source of the plasma belt to be the solar wind coming from the current sheet, entering the inner magnetosphere by the magnetospheric flanks.

6. Plasma energization

The initial analysis of the plasma belt structure has shown a significant increase of plasma temperature in the inner magnetosphere (see panels c, f, and i in Figures 2 and 3). The increased plasma temperature thus indicates that effective heating and/or acceleration of precipitating solar wind protons takes places inside the Hermean magnetosphere similarly to the terrestrial case.

In order to demonstrate and quantify the energization processes we plot in Figure 7 the proton energy distributions derived from the simulation NIMF-P for three distinct locations, i.e., the unperturbed solar wind plasma in front of the bow shock (marked with black triangles), the plasma sheet at the predefined point N3, and finally the nightside plasma belt at the point N1 (see panel a in Figure 2 for reference). For a quantitative comparison the energy distributions are further over plotted by Maxwellian distributions (solid, dashed, and dotted line for the solar wind, plasma belt, and plasma sheet respectively) having corresponding bulk plasma properties derived at the individual locations. We use the Maxwellian distribution for simplicity although in the section 4 we have shown that different, like loss-cone distributions are present in the inner magnetosphere. It is important to note that the evaluation of the bulk plasma properties, i.e., the density n, temperature T, and bulk speed v_b as shown in Figure 7, is restricted to the energy range where the derived distributions follow the Maxwellian prediction.

Comparing the bulk properties of the three populations, we can see that the plasma sheet population (N3) has approximately three times lower temperature than the population from the quasi-trapped region in the plasma belt (N1). On the contrary the bulk speed is approximately almost four times larger, in the plasma sheet the population travels with approximately Alfvén velocity (in the solar wind $v_{A\mathrm{sw}}$) towards the northern dawn sector. The bulk speed of the proton population at point N1 is about 1/3 of the solar wind

protons Alfvén speed (v_{Asw}). Both the plasma sheet and plasma belt protons are significantly heated with a respect to the impacting solar wind flow. While the solar wind protons, as given by the simulation setup, have typical energies above 1 keV (being a composition of the internal thermal energy and kinetic energy provided by the solar wind flow) the energy distribution for the plasma belt population shows a significant fraction of the protons at energies up to several keV and in the simulations we observe particles having energies even higher than 10 keV. Comparing the high energy proton densities given by the plasma belt distribution with the solar wind protons it is also obvious from Figure 7 that the high energy particles can not be simply explained as a result of some velocity filtration effects of the solar wind protons but these must be effectively heated or accelerated inside the Hermean magnetosphere. The energization can be explained by the particle trapping in the closed field lines similar to the effect in radiation belts region at Earth. It is also important to note that the energy distributions of both the plasma belt and plasma sheet populations develop clear high energy non-thermal tails which deviates from the thermal part described by the Maxwellian distribution.

The plasma energization process in the Hermean magnetosphere is further demonstrated in the two lower panels of Figure 6. Here we plot the proton temperature (solid line in the middle panel), density (dashed line in the bottom panel), and bulk speed (solid line in the bottom panel) as a function of the distance along the plasma flowline ending in the point NM2. The vertical dashed lines correspond to numbered positions indicated in the top panels. We can clearly identify the plasma deceleration and compression when crossing the bow shock (point 1), plasma acceleration towards the planet within the current/plasma sheet (point 2), and significant heating of the plasma when entering the plasma belt region (point 3). At point 3, the bulk velocity drops significantly as the planetward flow in the constrained current sheet is dispersed into wide region of the plasma belt. Moreover, protons coming from the tail experience heating as they enter the plasma belt region. Part of the kinetic energy gained in the tail is transferred into thermal energy.

Overall proton plasma bulk properties at all the individual predefined points in the simulation box for both the NIMF-P and SIMF-P configurations are summarized in Table 4 in comparison to the initial solar wind conditions. In the nightside the proton properties are found to be comparable between the north IMF (points N1, N2, and N3) and the south IMF configuration (points S1, S2, and S3). Clear difference is found for the dayside (poins N4 an S4) where the plasma belt region is significantly restricted in the SIMF-P case as already indicated in section 4 (see Figures 2 and 3).

7. Quasi-trapped particles (NIMF-P)

As has been shown in case of the NIMF-P simulation, the planet possesses a larger dayside magnetosphere compared to SIMF-P with a significant proton population that exhibits a loss cone distribution with higher energies suggesting the existence of a quasi-trapped particles population. We therefore in the following study focus only on the NIMF-P simulation case. The region with enhanced temperatures fills the dayside magnetosphere and on the nightside extends up to $\approx 1.5R_M$ above the planetary surface. The form is similar as in the case of Earth, i.e., toroidal shaped structure confined to a magnetic shell.

We have performed test particle simulations in order to observe the behavior of single particles. At the point N1 the test particles (protons) were injected with initial velocities equal to velocities of VDF computed at this point. In total about 12 thousand particles, representing the acquired velocity distribution function, were injected into the simulated magnetic and electric field. Of this quantity, 67% ended on the Hermean surface, 29% left the simulation box and 4% reached the maximum number of iterations arbitrarily set for the test particle simulation.The particles reaching the maximum iteration number mainly ended elsewhere in the magnetospheric tail, leaving also the plasma belt.

Two examples of trapped particles are shown in the left panel of Figure 8 with solid line showing the particle trajectory. One particle was injected from the point N4, ahead of the planet (blue line). This particle has been initiated with velocity $v = (-1.25, -4.20, -4.16)v_{Asw}$, being a suprathermal particle with energy of 2.4 keV (see the bulk properties in Table 4). It can be seen that the particle gyrate around the magnetic field lines, having quite a large Larmor radius. Furthermore, the particle drifts clock-wise (as seen from the north pole) around the planet due to a combined grad B and curvature drift. Finally the particle hits the planetary surface after $\sim 1/4$ orbit around the planet.

Similar behavior can be observed in the case of the second example test particle that was injected at the point NM2. At this point, in total about 10 thousand particles were injected. 98% of this quantity ended on the Hermean surface, 2% left the simulation box and 9 particles have reached the iteration maximum. The red line in the left panel of Figure 8 shows the second test particle example. This particle was injected with the velocity of $v = (2.49, -3.63, -4.06)v_{Asw}$, with similar energy as the first particle (~ 2.4 keV).

Additionally, the test particles from points N1, N3, and NM1 were injected using respective VDF for their initial velocities in order to have different sources around the planet. The point N1 being at the nightside within the plasma belt, N3 at the nightside outside of the plasma belt, and NM1 at the dawn side of the planet. The right panel of Figure 8 displays the end points of all the particle trajectories from N1 (blue), N3 (red), N4 (magenta), NM1 (green), and NM2 (yellow) that ended on the Hermean surface. The figure shows the Hermean surface in cylindrical equidistant projection with background of the Hermean surface image compiled from MESSENGER observations and provided by NASA (http://www.nasa.gov/mission_pages/messenger/main/). Zero meridian corresponds to the nightside and 180° meridian to the dayside of the planet.

All the test particle impact locations together create on the surface similar pattern as the precipitating protons from the corresponding simulation itself shown in Figure 1e. The pattern results from the magnetic field lines configurations and the respective trapped particle region. At the dayside, the region of quasi-trapped particles is wider in terms of latitude, because the magnetic field here is compressed by the incoming solar wind. The sub-solar point of the planetary surface and adjacent region is shielded by Hermean magnetic field and almost no particles penetrate to this region. When going to the nightside, the field lines are elongated enabling the particle trapping mechanism to take place at lower latitudes. At the nightside (near 0° meridian) the particles precipitate at low magnetic latitudes. Here, at the nightside (0°), a shift towards north pole of the planetary dipole is visible. The southern boundary of the protons hitting the surface is around 35° of southern latitude, while on the other hemisphere, it is around 50° of northern latitude.

The view is also consistent with theoretical expectations that stem from the dipole northward offset. The offset means that near the northern pole, the surface magnetic field is stronger and on the southern pole weaker. Then the southern hemisphere should be more under bombardment of solar wind particles. This is also visible at the right panel of Figure 8, that clearly shows higher amount of particles on the southern hemisphere. When quantifying it, about 58% of all particles shown hit the southern hemisphere.

Table 4. Bulk proton population properties at points N1, N3, N4, NM1, and NM2 for the NIMF-P simulation, points S1, S2, S3, and S4 for SIMF-P simulation, and for undisturbed solar wind distribution that enters the simulation (SW). Points positions are indicated in Figure 2 and 3.

Property	**SW**	**N1**	**N2**	**N3**	**N4**	**NM1**	**NM2**	**S1**	**S2**	**S3**	**S4**
Density n_p $[cm^{-3}]$	15	8.3	8.1	8.0	8.0	16	8.8	9.0	8.0	6.8	0.04
Bulk speed magnitude $\|v_b\|$ [$v_{A\mathrm{sw}}$]	4	0.47	0.54	1.0	0.24	0.42	0.1	0.25	0.85	2.4	0.93
Thermal speed v_{th} [$v_{A\mathrm{sw}}$]	0.87	4.8	4.0	2.5	4.1	3.5	5.7	4.6	3.3	2.9	6.6
Mean energy $\langle E \rangle$ [keV]	1.1	1.8	1.2	0.50	1.3	0.89	2.5	1.5	0.81	0.97	3.1

We can identify the different origin of the particles by the color code. Color dots are generally grouped together and localized on the Hermean surface with smaller amount of scattered points. It shows also that the test particles hit the surface close to their injection point, while drifting of about 1/4 of the full orbit around the planet. Particles are more likely only quasi-trapped, meaning, that soon they hit the surface or leave. This is likely the effect of dimensions of the magnetosphere with respect to the Larmor radius that is quite large and a gyrating proton sees different magnetic field magnitudes even during one gyration. Particles will also undergo pitch angle diffusion and scattering. The particles originating from within the plasma belt (points N1-blue, N4-magenta, NM1-green, and NM2-yellow) are more localized (grouped together) than the endpoints of the particles originating in the point N3 (red) positioned further in the tail. The particles originating at point N3 in the plasmasheet are scattered across all longitudes mainly in high latitudes, where the field lies from the plasmasheet are connected and the field aligned currents can appear.

8. Comparison of the simulated data to in situ measurements

The MESSENGER spacecraft was inserted in the Hermean orbit on March 18, 2011. We use magnetometer data from the MAG instrument [*Anderson et al.*, 2007] and data from the plasma spectrometer FIPS [*Andrews et al.*, 2007]. Data are available through the Planetary Data System (http://pds-ppi.igpp.ucla.edu/). MESSENGER uses Mercury Solar Orbiter (MSO) coordinates, defined as X_{MSO} directed from the center of the planet toward the Sun; Z_{MSO}, normal to Mercury's orbital plane and positive toward the north celestial pole; and Y_{MSO}, positive in the direction opposite to orbital motion [*Slavin et al.*, 2008]. In the simulations we use rather Solar Hermean Orbital (SHO) coordinate system, where the $\mathcal{X}$ axis is directed in the solar wind flow direction, the $\mathcal{Z}$ axis is formed by the planetary rotational axis directed northward, and the $\mathcal{Y}$ axis lies in the equatorial plane forming the right-handed coordinate system. Within this study, all data and trajectories are converted into the SHO coordinate system.

We have chosen data from part of the MESSENGER orbit from 2011-07-01 (day 182) in particular from 2011-07-01T06:27:52 until 2011-07-01T09:44:52. The orbit is almost in the noon-midnight plane with the perihermion on the nightside around 45° of the northern latitude. This orbit crosses the cusp region on the dayside and enables us to study the plasma ring current at the nightside. Figure 9 shows selected trajectory (in black) with focus (red) on the nightside crossing of the ring current region. The highlighted section of the orbit lasts from 2011-07-01T07:28:13 until 2011-07-01T07:46:08. The trajectory is over-plotted on the density data of the NIMF-P simulation run. This simulation has been chosen according to matching initial parameters to the solar wind condition at Mercury during the observations period used. In particular the IMF from MESSENGER MAG data was: $B_x = 17.33$ nT , $B_y = 0.04$ nT, $B_z = 4.15$ nT. These values were calculated as an average from selected MAG data before the bow shock crossing.The IMF was therefore northward with angle of 13.47° between the IMF direction and the sub-solar line. The simulation NIMF-P has the IMF set-up corresponding to $B_x = 18.79$ nT, $B_y = 0.0$ nT, $B_z = 6.84$ nT with 20° between the IMF direction and the sub-solar line.

Figure 10 shows data along the selected trajectory (as presented in Figure 9). Panel a shows the proton density along the virtual MESSENGER trajectory through the simulated data. Panel b shows the magnetic field measured by MAG (blue line), the magnetic field from the simulation along the same trajectory (in red), and the magnetic field fluctuations computed from the MAG measurements are in the background. Panel c shows data acquired by the FIPS instrument and gives the spectrogram of high energetic ions (FIPS SCAN mode). FIPS was measuring during the whole period shown, however, at some points no counts were detected. All panels have a highlighted region from 7:28 to 7:46 UTC that corresponds to the density increase in the inner magnetosphere indicating the ring current region. This density increase is accompanied by a diamagnetic decrease visible in the magnetic data (simulated as well as measured). Moreover FIPS data indicate the presence of plasma and high energetic ions, a signature of the quasi-trapped particles. The presence of such particles was already reported by *Schriver et al.* [2011].

MESSENGER data (MAG and FIPS) indicate crossing of various magnetospheric regions. At the beginning of the time period displayed, the MESSENGER spacecraft is in the solar wind in the foreshock region (below the equatorial plane towards south), entering the magnetosheath above the equatorial plane at around 6:57 as indicated by enhanced lower energy proton observations in panel c as well as enhanced magnetic field fluctuations. There is a good correspondence also with the simulated density (panel a) and the magnetic field data (panel b - red curve) that shows the bow shock crossing at this time. Crossing the magnetosheath, the spacecraft enters the dayside magnetopause at 7:06. The magnetopause (MP) crossing is noted by the suppression of the magnetic fluctuations and the lack of magnetosheath low energy protons. The MP crossing is followed by the observations of higher energetic protons indicating low latitude boundary layer (LLBL) presence, which is likely merged with the trapped particle region as discussed above based on the simulation results. The dayside crossing neither the LLBL can not be observed in simulation data. As it is clear from the trajectory plot over data in Figure 9, the path does not cross the dayside magnetosphere in the simulation, but via cusp region enters magnetospheric northern lobe. This discrepancy between the simulation and measurement would indicate, that the simulation set-up has a higher solar wind ram pressure compared to the real conditions. The higher solar wind ram pressure would suppress the dayside magnetosphere towards the planet. In the real data, the spacecraft goes through the cusp region at 7:17 indicated by the FIPS measurements as well as by the magnetic fluctuations. This crossing correlates with the peak in simulated proton density. Then the spacecraft enters the northern lobe (for the in situ measurements as well in the simulation data set).

From 07:28 to 07:46, as highlighted by the green rectangle, the simulations data show an increased proton density

and a drop in the magnetic field. The drop is visible also in measured magnetic field (panel b blue line). The highlighted region exhibits high energy protons (in the FIPS range 2 to 14 keV). Comparable proton energies are equally observed in the plasma belt in the simulated data as it was shown in section 6 (c.f., Figure 7 and Table 4). Aforementioned aspects indicate that the spacecraft in this part of the orbit crossed the nightside plasma belt with quasi-trapped energetic particles.

Later on, the measurements were taken in the southern magnetospheric lobe, entering the magnetosheath at around 8:22 in the boundary layer followed by the 8:29 MP crossing. The MP data crossing in simulated data is slightly postponed to the real measurements, that would indicate broader nightside magnetospheric structure for the simulation dataset, which is in line with the assumption of the higher plasma pressure in the simulation compared to the real conditions. At about 8:55 UTC the FIPS instrument switched from the burst into normal mode, having afterwards lower time resolution but higher integration time. It shall be noted, that the FIPS instrument has a limited field-of-view, hence the solar wind proton counts are not fully representative. However, in the magnetosheath the protons are thermalized and have a low bulk velocity and therefore the FIPS data can be used for the magnetosheath identification.

9. Discussion

The simulations as well as in situ data indicate that Mercury possesses a plasma belt region with a quasi-trapped population. We have shown the general structure of this region using numerical simulations by comparing the simulation runs with different IMF orientations. The plasma belt region is characterized by the increase in the ion temperatures and the observation of quasi-trapped particles. These particles are not able to drift around the whole planet, due to the small scales of the magnetosphere and to form a steady ring current as it is the case at Earth. At Mercury, the plasma belt protons drift only along the part of the orbit and then either hit the surface or leave the inner magnetosphere. Therefore we talk about quasi-trapped particles. A portion of these particles precipitate onto the planetary surface. The pattern of the precipitation is asymmetric for the southern and northern hemisphere. The plasma belt is constantly supplied by the solar wind ions coming from the magnetospheric flanks and tail.

There are several phenomena related to the plasma belt and its population, that shall be discussed in a broader context.

At first, it is the validity of the numerical simulation. The simulated Mercury is, due to the limited computational resources, downscaled with the factor of ∼1.9, preserving however the magnetopause stand-off distance. Therefore, the global magnetospheric dimensions shall be correct relatively to the planet dimensions. This has been also demonstrated by the comparison of the simulations with the real in situ measurements that show a very good agreement. The feature, that might slightly influence the results, is the local behavior of the protons, as the Larmor radius in real situation would be smaller. This will probably influence only the total amount of the precipitation protons and might increase the trapping mechanism. The general results and the precipitation pattern shall be representative. For example, the fact that the precipitation in case of Mercury is highly asymmetric in northern and southern hemisphere is valid. The precipitation asymmetry will probably affect the surface and related processes, such as electron stimulated desorption and solar wind sputtering. It shall be noted, that surface related processes such as back scattering of the incoming protons or solar wind sputtering are not implemented in the simulation code. For example the back scattering of the protons from the surface might influence the proton populations near the surface. However, as learned from the Lunar regolith properties [*Lue et al.*, 2014], the portion of the backscattered protons is probably rather small ($< 1\%$). The effect shall be studied in more detail in further research also comparing the in situ data.

For different orientation of the IMF, the precipitation pattern differs. As a result, the pattern asymmetry differs for the IMF directed planetward (IMF $B_x > 0$) and sunward (IMF $B_x < 0$). The location of the reconnection in these two cases is driving not only the access of the solar wind plasma to the cusp regions, but it also affects the current sheet in the tail. The sketch in Figure 11 compares two cases of the IMF orientation (the planetward IMF in panel a and the sunward IMF in panel b). With the blue dashed ellipses, the locations of favorable conditions for the reconnection are indicated. The shaded area indicates a plasma mantle location and the red arrow expected curvature force direction. For the sunward IMF (panel b), the reconnection in the tail can take place predominantly in the southern lobe. This can lead to the magnetic flux removal from the southern lobe and decrease in magnetic pressure. As a consequence, the current sheet would shift towards south. For the planetward IMF case (panel a) the situation is analogous, but the reconnection in the tail is happening in the northern lobe. Therefore also particles coming from the tail current sheet, have asymmetric access to the planetary hemispheres.The reconnection assymetry has also effect on the plasma mantle location. For planetward IMF, the plasma mantle appears predominantly in the northern lobe, while in case of sunward IMF, thicker and more populated mantle appears in southern lobe. The feature again driven by the reconnection location and the solar wind particle access to the inner magnetosphere as presented in more detail by *Herčík* [2013]. Moreover, there is also a dependence of the plasma mantle appearance on the north-south IMF component [cf. *Sckopke et al.*, 1976], where the plasma mantle appears predominantly for northward IMF. This feature is also visible in our simulations and supports the idea of the reconnection location importance and the solar wind protons access to the inner magnetosphere.

The precipitation IMF dependence effect seems to be quite strong, as the results of proton precipitation from the simulation show. Also the current sheet shift is strongly visible in the simulations and depends on the IMF B_x component only. Additionally, the dipole shift plays significant role as well for the precipitation itself.

Another interesting fact to be mentioned is the energy of quasi-trapped particles.

The analysis of the simulation results shows protons with energies of even about ∼10 keV forming supra-thermal tails of the energy distribution functions. Of course the simulation does not include all the sources for high energetic particles. Actually the only source of the protons is the solar wind that is partially energized in the tail and further more around the planet in the plasma belt. The means of energization can be the cross tail potential in the tail and wave-particle interaction in the plasma belt region, where plasma waves can be generated due to the anisotropic plasma distribution. When looking at the Earth's radiation belt population for comparison, several phenomena are missing in our simulations: galactic cosmic rays, solar energetic particles, or Hermean exosphere.

However, even the MESSENGER data show, that there is a deficiency in the high energetic particles. As *Schriver et al.* [2013] presented, the high energetic particles (> 100 keV) are rather exceptional in the Hermean magnetosphere. They suggest various reasons for this feature. The energization processes are different mainly due to the different scales, that shall result in the low cross tail potential or distance

from the tail current sheet reconnection location to the planet. The plasma belt region itself is much smaller and therefore, there is not enough space and plasma for larger wave activity to develop and to transfer the energy to the particles. Moreover the plasma belt particles are being trapped in the region for a short time only and after several bouncing periods usually leave the region. Therefore there is not much time for further energization.

The very high energetic (> 10 MeV) part of the spectra at Earth comes from the galactic cosmic ray interaction with the atmospheric atoms producing neutrons that undergo decay [*Panasyuk*, 2004]. In the case of Mercury, there is only a tenuous exosphere, so it means that the very high energetic particles are not probable to be found.

To conclude, we have provided an analysis of the simulated plasma belt at Mercury with its properties, structure, and several interesting features. A further analysis of the region, including electron test particle simulations, analysis of the local wave-particle interaction within the loss cone plasma distributions, or estimation of the effect of the particle precipitation to the planetary surface in terms of exosphere formation will follow.

Acknowledgments. Magnetic field data used: MESS-E/V/H/SW-MAG-3-CDR-CALIBRATED-V1.0, plasma data used: MESS-E/V/H/SW-EPPS-3-FIPS-CDR-V1.0. Both datasets obtained by Planetary Data System (PDS). The simulation data used within the study are accessible through the Virtual Mission Laboratory Portal (http://amalka.asu.cas.cz/). The research leading to these results has received funding from the European Commission's 7th Framework Programme under the grant agreement #284515 (project-shock.eu).

References

Anderson, B. J., M. H. Acuña, D. A. Lohr, J. Scheifele, A. Raval, H. Korth, and J. A. Slavin (2007), The Magnetometer Instrument on MESSENGER, *Space Sci. Rev.*, *131*(1-4), 417–450, doi:10.1007/s11214-007-9246-7.

Anderson, B. J., et al. (2011), The Global Magnetic Field of Mercury from MESSENGER Orbital Observations, *Science*, *333*(6051), 1859–1862, doi:10.1126/science.1211001.

Andrews, G. B., et al. (2007), The Energetic Particle and Plasma Spectrometer Instrument on the MESSENGER Spacecraft, *Space Sci. Rev.*, *131*(1-4), 523–556, doi:10.1007/s11214-007-9272-5.

Ashour-Abdalla, M., et al. (1998), Determination of Particle Sources for a Geotail Distribution Function Observed on May 23, 1995, in *Geosp. Mass Energy Results From Int. Solar-Terrestrial Phys. Progr.*, *Geophysical Monograph Series*, vol. 104, edited by L. Horwitz, L. Gallagher, and K. Peterson, geophysica ed., pp. 297–312, American Geophysical Union, Washington, D. C.

Daglis, I. A. (1997), Terrestrial agents in the realm of space storms: Missions study oxygen ions, *Eos Trans. AGU*, *78*(24), 245, doi:10.1029/97EO00162.

Daglis, I. A., R. M. Thorne, W. Baumjohann, and S. Orsini (1999), The terrestrial ring current: origin, formation, and decay, *Rev. Geophys.*, *37*(4), 407– 438.

Delcourt, D. C., S. Grimald, F. Leblanc, J.-J. Berthelier, A. Milillo, A. Mura, S. Orsini, and T. E. Moore (2003), A quantitative model of the planetary Na+ contribution to Mercury's magnetosphere, *Ann. Geophys.*, *21*, 1723–1736, doi:10.5194/angeo-21-1723-2003.

Dunne, J., and E. Burgess (1978), *The Voyage of Mariner 10 - Mission to Venus and Mercury*, vol. 214, 232 pp., NASA, Washington, DC, doi:10.1038/scientificamerican0366-42.

Goldstein, B. E., S. T. Suess, and R. J. Walker (1981), Mercury: Magnetospheric Processes and the Atmospheric Supply and Loss Rates, *J. Geophys. Res.*, *86*(A7), 5485–5499, doi:10.1029/JA086iA07p05485.

Herčík, D. (2013), Planetary investigation by global numerical simulations: Study of Hermean environment, Ph.D. thesis.

Herčík, D., P. M. Trávníček, J. R. Johnson, E.-H. Kim, and P. Hellinger (2013), Mirror mode structures in the asymmetric Hermean magnetosheath: Hybrid simulations, *J. Geophys. Res. Sp. Phys.*, *118*(1), 405–417, doi:10.1029/2012JA018083.

Hultqvist, B., M. Oieroset, G. Paschmann, and R. A. Treumann (1996), Plasma transfer processes at the magnetopause, in *Magnetos. plasma sources losses*, edited by B. Hultqvist, M. Ø ieroset, G. Paschmann, and R. Treumann, chap. 5, pp. 207–283, Springer Science+Business Media Dordrecht.

Leblanc, F., and R. E. Johnson (2003), Mercury's sodium exosphere, *Icarus*, *164*(2), 261–281, doi:10.1016/S0019-1035(03)00147-7.

Lue, C., Y. Futaana, S. Barabash, M. Wieser, A. Bhardwaj, and P. Wurz (2014), Chandrayaan-1 observations of backscattered solar wind protons from the lunar regolith: Dependence on the solar wind speed, *J. Geophys. Res. Planets*, *119*(5), 968–975, doi:10.1002/2013JE004582.

Moore, T. E., et al. (2005), Plasma sheet and (nonstorm) ring current formation from solar and polar wind sources, *J. Geophys. Res. (sp. Physics)*, *110*, 2210, doi:10.1029/2004JA010563.

Morgan, T. H., and R. M. Killen (1997), A non-stoichiometric model of the composition of the atmospheres of Mercury and the Moon, *Planet. Space Sci.*, *45*(1), 81–94, doi:10.1016/S0032-0633(96)00099-2.

Panasyuk, M. I. (2004), The Ion Radiation Belts : Experiments and Models, in *Eff. Sp. Weather Technol. Infrastruct.*, edited by I. A. Daglis, pp. 65–90, Kluwer Academic Publisher.

Paral, J., P. M. Travnicek, R. Rankin, and D. Schriver (2010), Sodium ion exosphere of Mercury during MESSENGER flybys, *Geophys. Res. Lett.*, *37*(19), 3–7, doi:10.1029/2010GL044413.

Richard, L. R., R. J. Walker, and M. Ashour-Abdalla (1994), The population of the magnetosphere by solar winds ions when the interplanetary magnetic field is northward, *Geophys. Res. Lett.*, *21*(23), 2455–2458.

Russell, C. T., D. N. Baker, and J. A. Slavin (1988), The magnetosphere of Mercury, in *Mercury*, edited by F. Vilas, C. R. Chapman, and M. S. Matthews, space scie ed., chap. 6, The University of Arizona press.

Sarantos, M., J. A. Slavin, M. Benna, S. A. Boardsen, R. M. Killen, D. Schriver, and P. M. Travnicek (2009), Sodium-ion pickup observed above the magnetopause during MESSENGER's first Mercury flyby: Constraints on neutral exospheric models, *Geophys. Res. Lett.*, *36*(4), 1–5, doi:10.1029/2008GL036207.

Schriver, D., et al. (2011), Quasi-Trapped Ion and Electron Populations at Mercury, *Geophys. Res. Lett.*, *38*, 1–6, doi:10.1029/2011GL049629.

Schriver, D., et al. (2013), What Happened to the High-Energy (> 100 keV) Particles at Mercury?, in *Am. Geophys. Union, Fall Meet. 2013, Abstr. #SM11E-02*.

Sckopke, N., G. Paschmann, H. Rosenbauer, and D. H. Fairfield (1976), Influence of the Interplanetary Magnetic Field on the Occurrence and Thickness of the Plasma Mantle, *J. Geophys. Res.*, *81*(16), 2687, doi:10.1029/JA081i016p02687.

Sckopke, N., G. Paschmann, G. Haerendel, B. U. O. Sonnerup, S. J. Bame, T. G. Forbes, E. W. Hones, and C. T. Russell (1981), Structure of the Low-Latitude Boundary Layer, *J. Geophys. Res.*, *86*(A4), 2099–2110.

Slavin, J. a., et al. (2007), MESSENGER: Exploring Mercury's Magnetosphere, *Space Sci. Rev.*, *131*(1-4), 133–160, doi:10.1007/s11214-007-9154-x.

Slavin, J. A., et al. (2008), Mercury's magnetosphere after MESSENGER's first flyby., *Science*, *321*(5885), 85–9, doi:10.1126/science.1159040.

Solomon, S. C., et al. (2001), The MESSENGER mission to Mercury : scientific objectives and implementation, *Planet. Space Sci.*, *49*, 1445–1465.

Song, P., and C. T. Russell (1992), Model of the formation of the Low-Latitude Boundary Layer for Strongly Northward Interplanetary Magnetic Field, *J. Geophys. Res.*, *97*(A2), 1411–1420.

Travnicek, P. M., P. Hellinger, and D. Schriver (2007), Structure of Mercurys magnetosphere for different pressure of the solar wind: Three dimensional hybrid simulations, *Geophys. Res. Lett.*, *34*, 1–5, doi:10.1029/2006GL028518.

Travnicek, P. M., D. Schriver, P. Hellinger, D. Hercik, B. J. Anderson, M. Sarantos, and J. A. Slavin (2010), Mercurys magnetospheresolar wind interaction for northward and southward interplanetary magnetic field: Hybrid simulation results, *Icarus*, pp. 1–12, doi:10.1016/j.icarus.2010.01.008.

Walker, R. J., L. R. Richard, and M. Ashour-Abdalla (1995), The Entry of Solar Wind ions Into the Magnetosphere, in *Phys. Magnetopause*, edited by P. Song, B. U. O. Sonnerup, and M. F. Thomsen, pp. 311–319, American Geophysical Union.

Yagi, M., K. Seki, Y. Matsumoto, D. C. Delcourt, and F. Leblanc (2010), Formation of a sodium ring in Mercury's magnetosphere, *J. Geophys. Res.*, *115*(A10), A10,253, doi: 10.1029/2009JA015226.

Petr Hellinger, Astronomical Institute, The Czech Academy of Sciences, Prague, CZ and Institute of Atmospheric Physics, The Czech Academy of Sciences, Prague, CZ

David Herčík, Astronomical Institute, The Czech Academy of Sciences, Prague, CZ and Institute of Atmospheric Physics, The Czech Academy of Sciences, Prague, CZ and Institute for Geophysics and Extraterrestrial Physics, Technical University, Braunschweig, DE (d.hercik@tu-bs.de)

Štěpán Štverák, Institute of Atmospheric Physics, The Czech Academy of Sciences, Prague, CZ and Astronomical Institute, The Czech Academy of Sciences, Prague, CZ

Pavel Trávníček, Space Sciences Laboratory, University California Berkeley, USA and Astronomical Institute, The Czech Academy of Sciences, Prague, CZ and Institute of Atmospheric Physics, The Czech Academy of Sciences, Prague, CZ

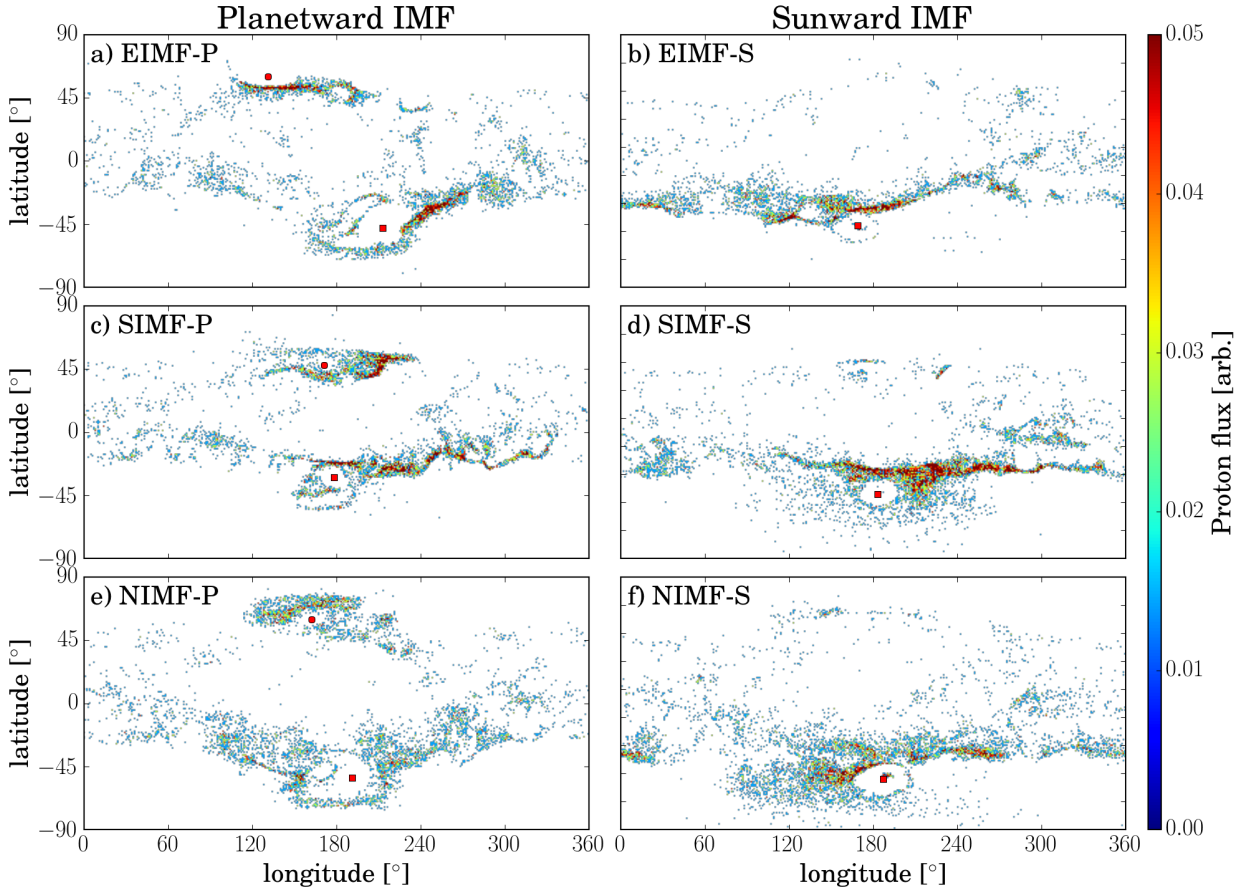

Figure 1. Proton fluxes (in arbitrary units) to the planetary surface are compared for all six simulation cases. Panel a shows the results for the simulation EIMF-P, b for EIMF-S, c for SIMF-P, d for SIMF-S, e for NIMF-P, and panel f for NIMF-S. The fluxes are mapped to longitude and latitude on the planetary surface. 0° longitude denotes the midnight meridian and 180° indicates the sub-solar meridian. 0° latitude is at the geographic equator, −90° denotes the south pole and +90° the north pole. The red squares (circles) indicate estimated southern (northern) cusp locations respectively.

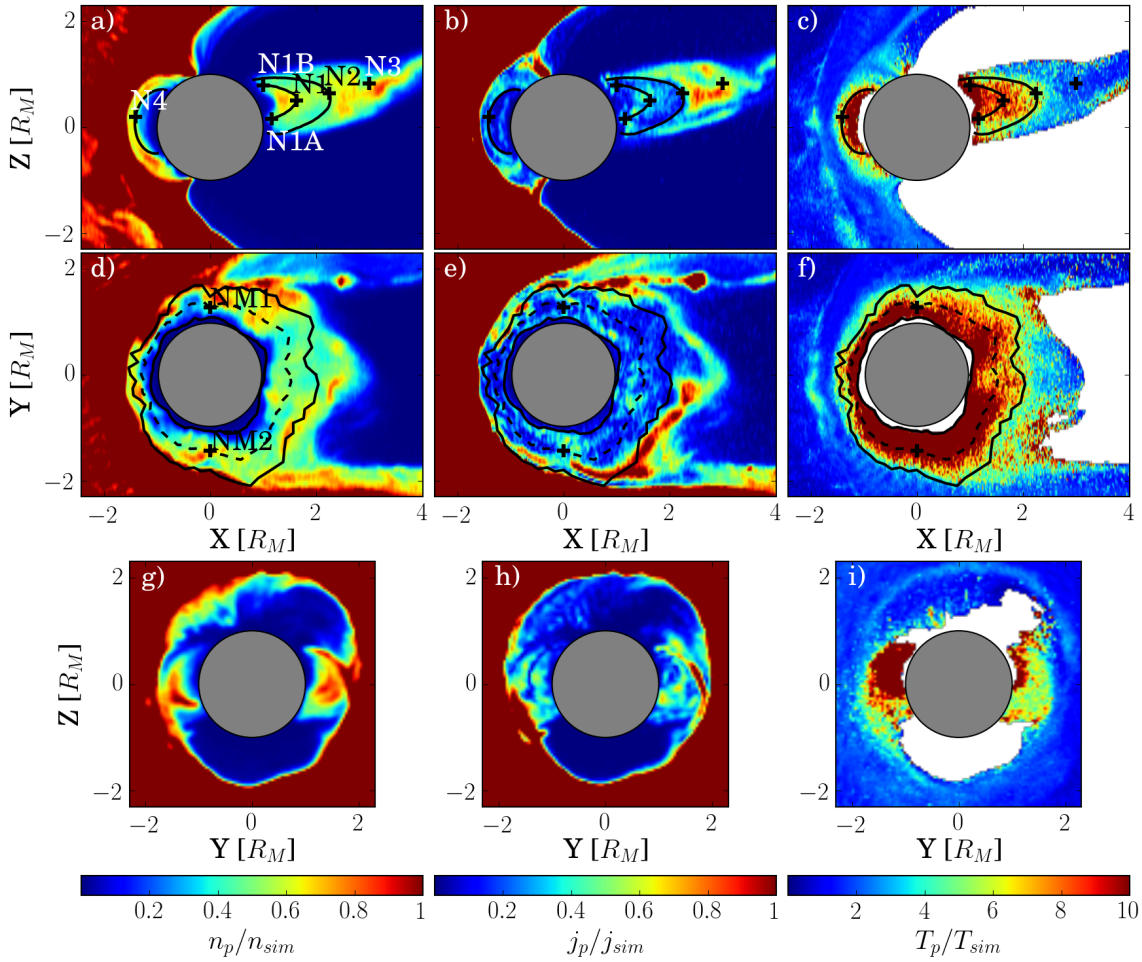

Figure 2. The general plasma belt structure for the NIMF-P simulation case. Panels a, d, and g show the proton particle density, panels b, e and h the proton current density and panels c, f, and i the proton temperature in the noon-midnight meridian (top panels a–c), magnetic equatorial (middle panels d–f), and dawn-dusk meridian plane (bottom panels g–i). All quantities are in simulation units. Black solid lines in the noon-meridian plane indicate particular field lines shown for a further reference as well as the black crosses indicate selected points. The black solid lines and the dashed line in panels d, e, and f show estimated boundaries and center of the plasma belt region. The white color in the temperature plots indicates places, where the density is too low to allow valid temperature computation.

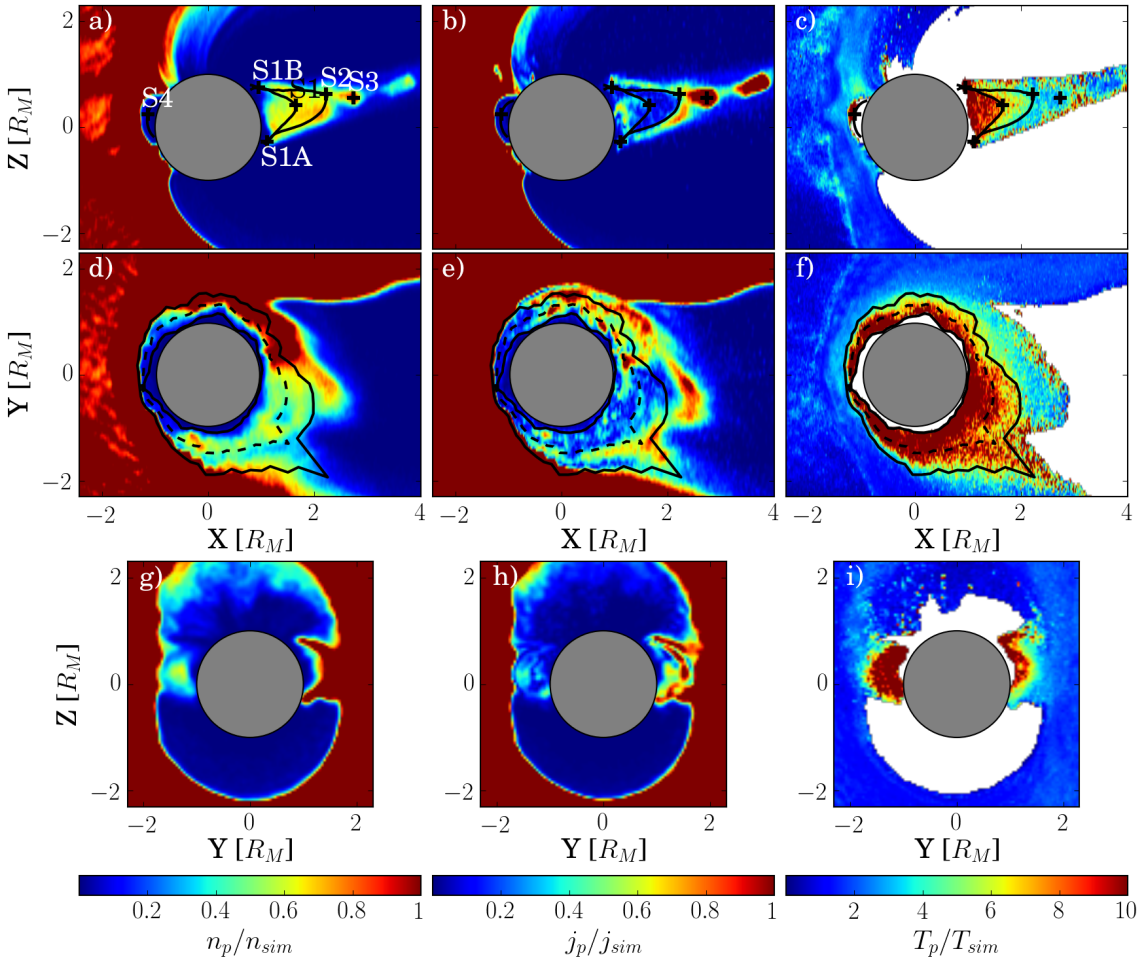

Figure 3. The general plasma belt structure for the SIMF-P simulation case. Panels a, d, and g show the proton particle density, panels b, e and h the proton current density and panels c, f, and i the proton temperature in the noon-midnight meridian (top panels a–c), magnetic equatorial (middle panels d–f), and dawn-dusk meridian plane (bottom panels g–i). All quantities are in simulation units. The black solid lines in the noon-meridian plane indicate the particular field lines shown for a further reference as well as the black crosses indicate selected points. The black solid lines and the dashed line in panels d, e, and f show estimated boundaries and center of the plasma belt region. The white color in the temperature plots indicates places, where the density is too low to allow valid temperature computation.

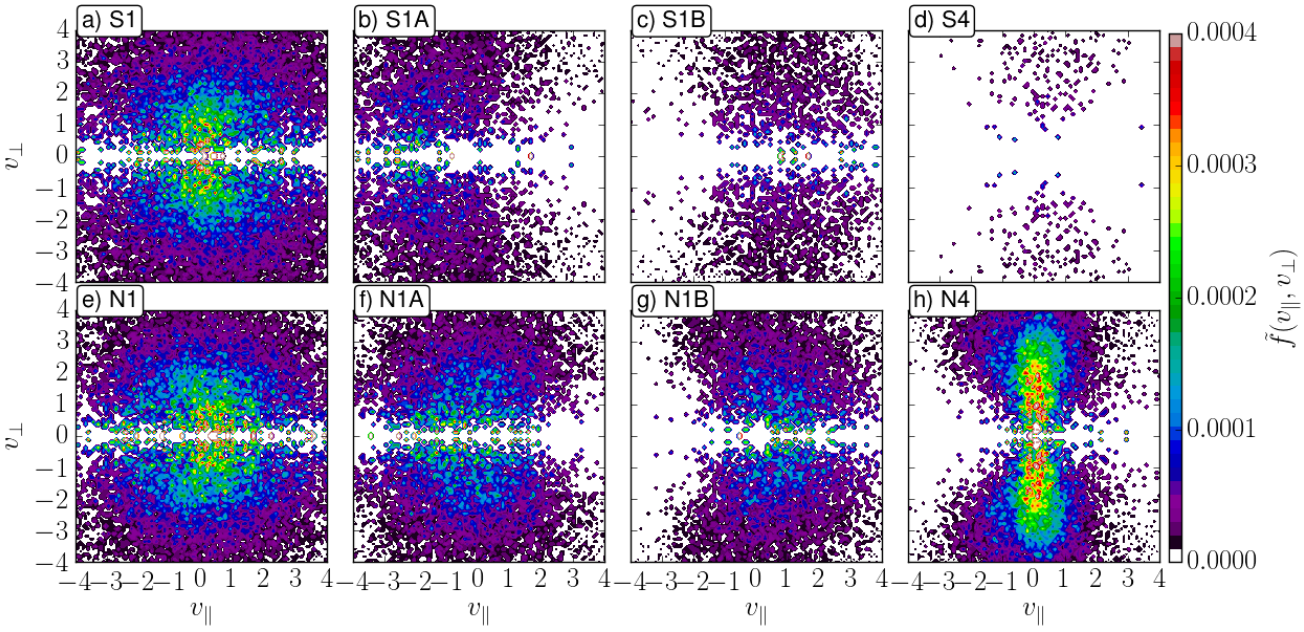

Figure 4. The normalized velocity distribution functions acquired at different locations. Top panels show the VDFs at points S1 (panel a), S1A (panel b), S1B (panel c), and S4 (panel d) from the SIMF-P simulation. Bottom panels show points N1 (panel e), N1A (panel f), N1B (panel g), and N4 (panel h) from the NIMF-P simulation. White color indicates no particles in the respective velocity phase-space acquired.

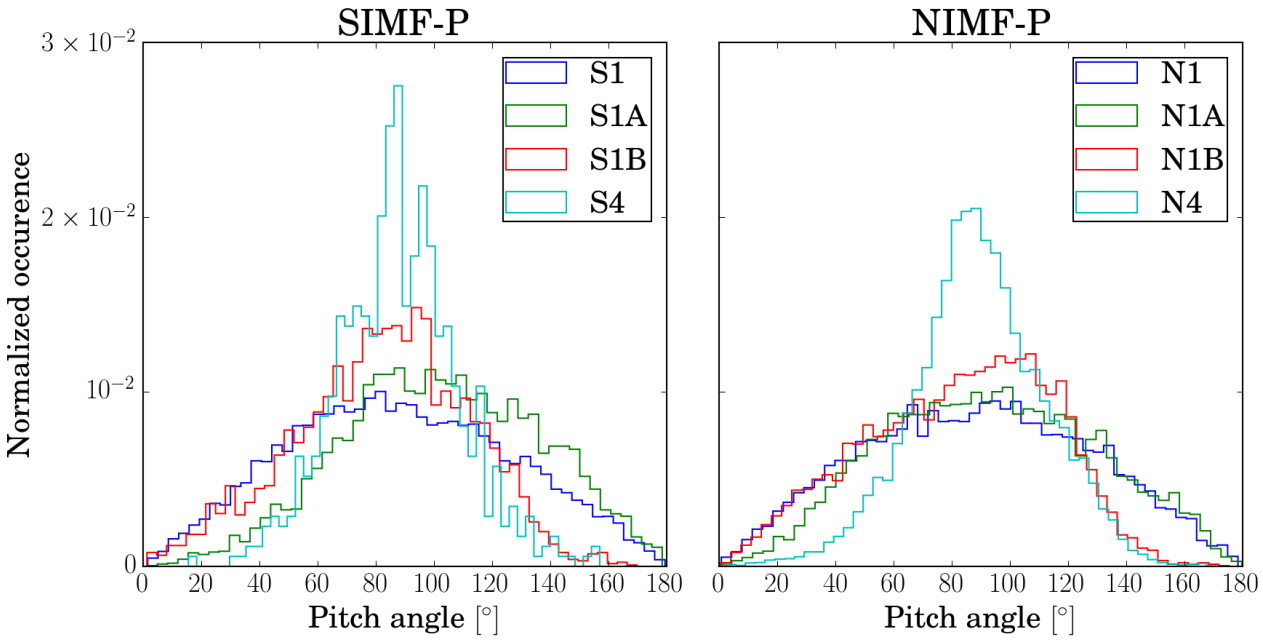

Figure 5. The pitch angle distribution functions acquired at different locations. The left panel shows PADs from the SIMF-P at points S1, S1A, S1B, and S4. The right shows PADs from the NIMF-P at points N1, N1A, N1B, and N4.

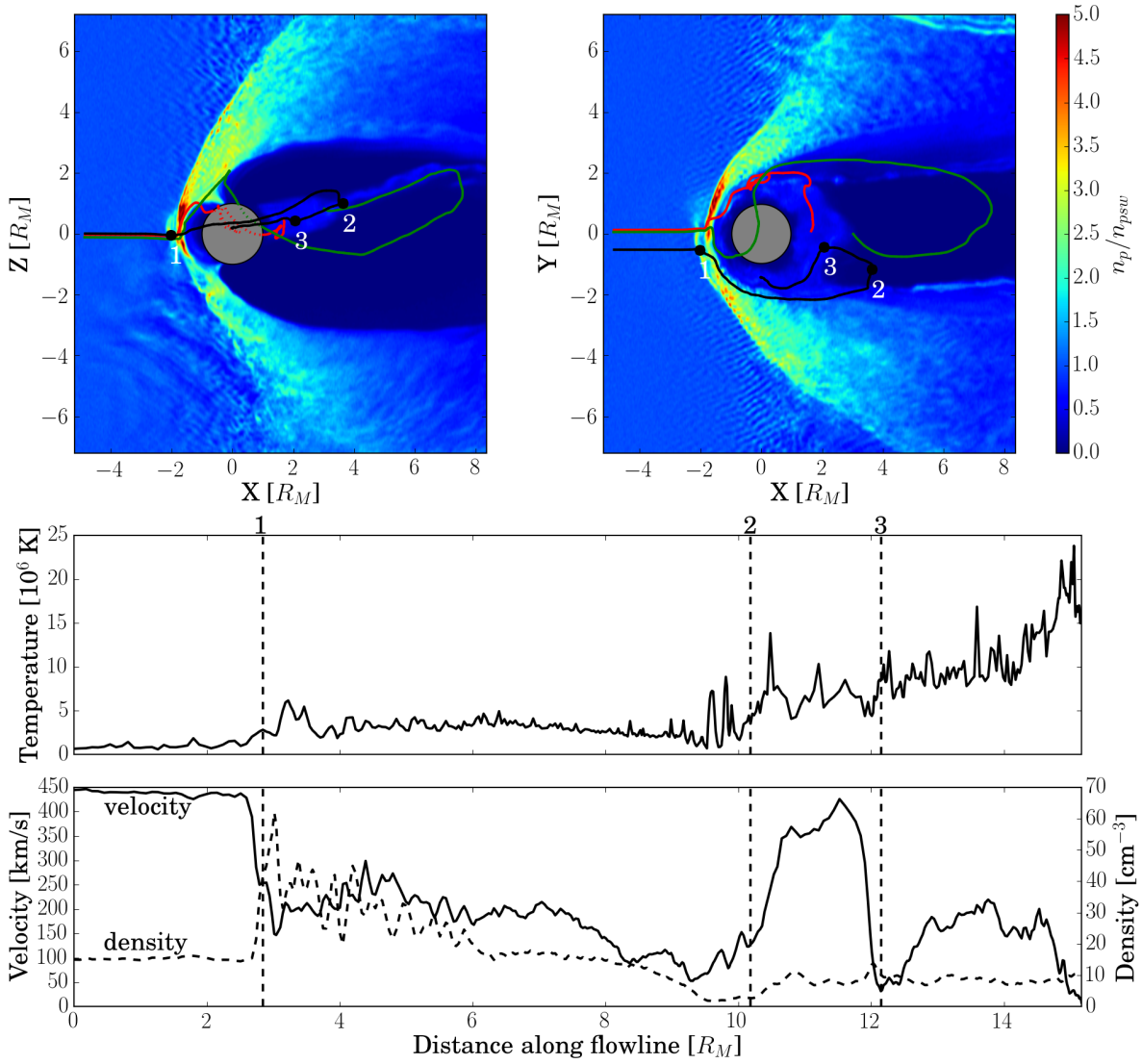

Figure 6. The plasma belt sources for the NIMF-P simulation. The color background shows the proton density in the noon-midnight meridian plane (upper left panel) and in the magnetic equator plane (upper right panel). The over-plotted solid color lines indicate examples of the flowlines computed from the bulk proton velocities with end point in the predefined points N1 (red), N4 (green), and NM2 (black). The dashed parts of the trajectories go behind the planet from the reader's viewpoint. The two lower panels display the characteristic proton bulk properties along the trajectory ending in the NM2 point. Vertical dashed numbered lines indicate locations of interest. Corresponding points in the space are shown by numbered black circles in the top panels. Particular features of the data along trajectories are discussed in detail in section 6.

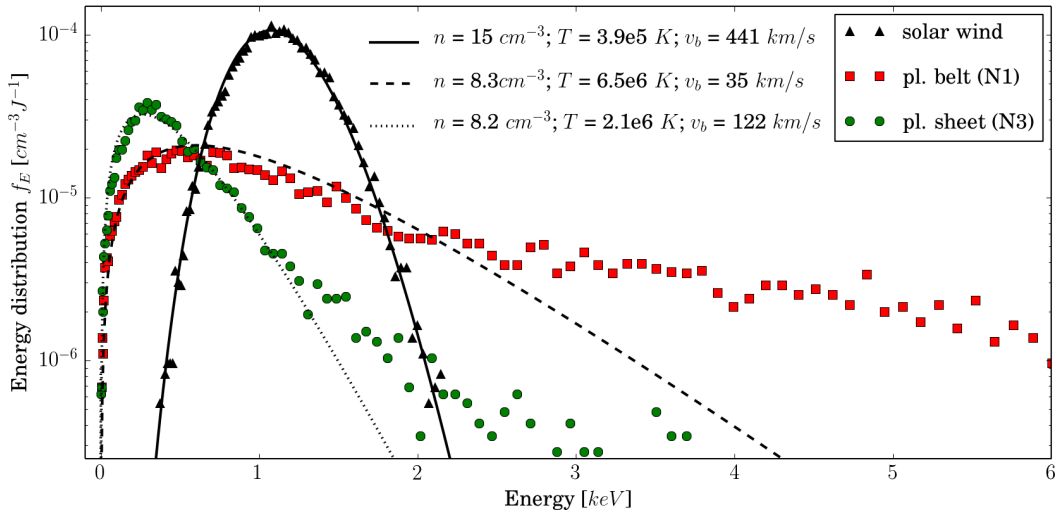

Figure 7. The proton energy distributions derived from the simulation NIMF-P are compared for selected locations. The markers show distributions for the free solar wind (black triangles), plasma sheet at N3 (green dots), and plasma belt on the night side at N1 (red squares). The energy distributions are over plotted by Maxwellian distributions (solid, dashed and dotted lines) having corresponding bulk plasma properties derived at the individual locations.

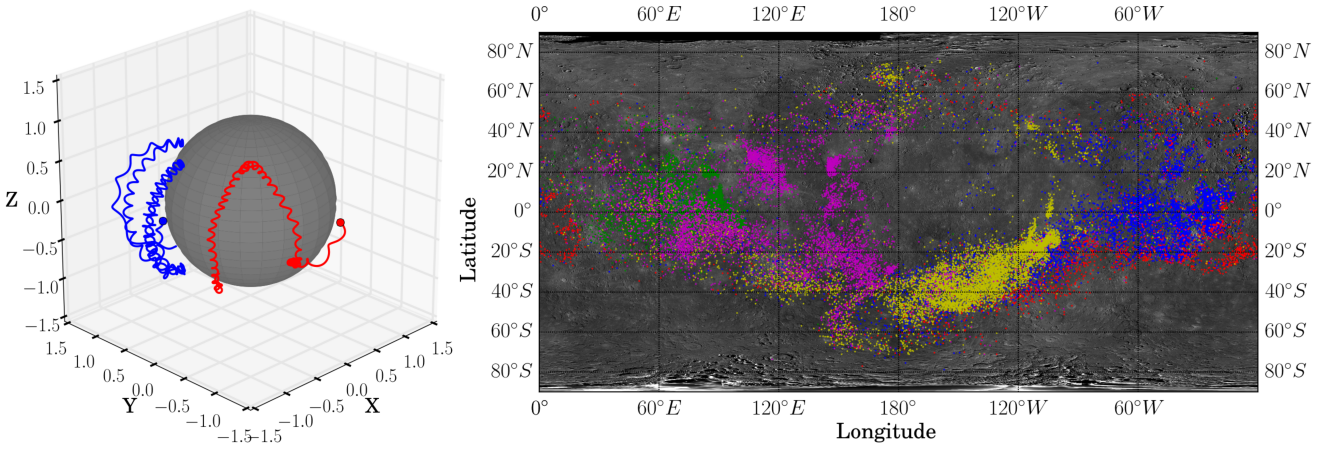

Figure 8. Left panel shows two examples of the test particles injected at point N4 (blue) and NM2 (red). Right panel shows test particle footprints, where the test particles collided with the planetary surface. The blue dots correspond to the particles originated at point N1, red at point N3, magenta at point N4, green at point NM1, and yellow at point NM2 as indicated in Figure 2. The background image credit: NASA/Johns Hopkins University Applied Physics Laboratory/Carnegie Institution of Washington. 0° longitude denotes the midnight meridian and 180° indicates the sub-solar meridian. 0° latitude is at the geographic equator, −90° denotes the south pole and +90° the north pole.

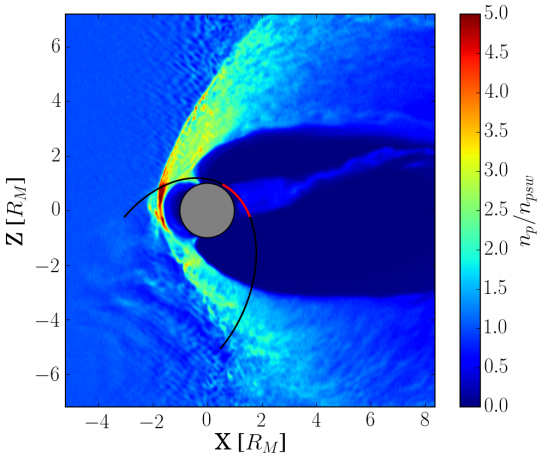

Figure 9. A part of the MESSENGER trajectory for day 182 in 2011 indicated by the black solid line. The trajectory is plotted on the proton density data from the NIMF-P simulation in the noon-midnight meridian plane. Part of the trajectory is highlighted by the red solid line for a further reference.

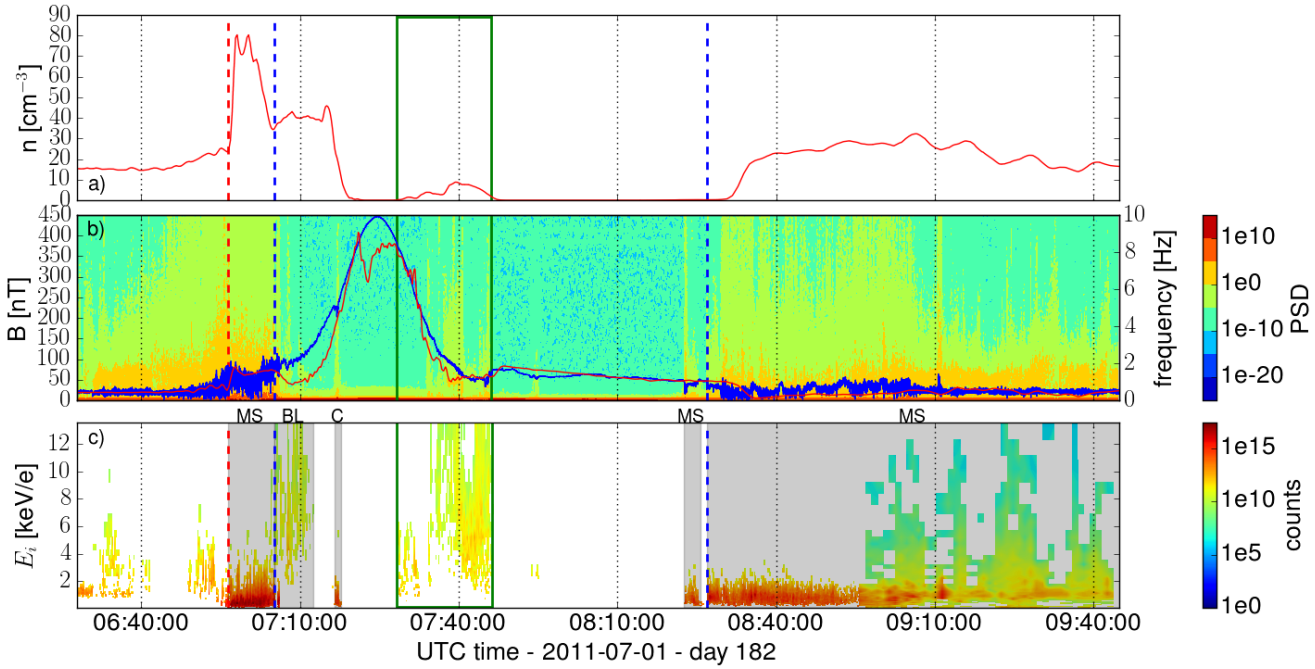

Figure 10. The comparison of MESSENGER data from the part of the orbit of day 182 in 2011 and simulated data along the same trajectory through the NIMF-P dataset. Panel a shows the simulated proton density. Panel b shows the simulated magnetic field intensity in red and in blue the real magnetic field measurements of the MESSENGER MAG instrument. The background shows power spectral density of the measured magnetic field. Panel c shows proton energies as measured by the MESSENGER FIPS instrument. The region bordered by the solid green line indicates part of the trajectory highlighted in Figure 9. The red dashed line indicates the estimated bow shock location and the dashed blue lines indicate estimated locations of the in and out bound magnetopause.Gray-shaded regions indicate periods, where the spacecraft was in magnetosheath ('MS'), magnetosheath boundary layer ('BL'), and cusp ('C') as derived from the FIPS data.

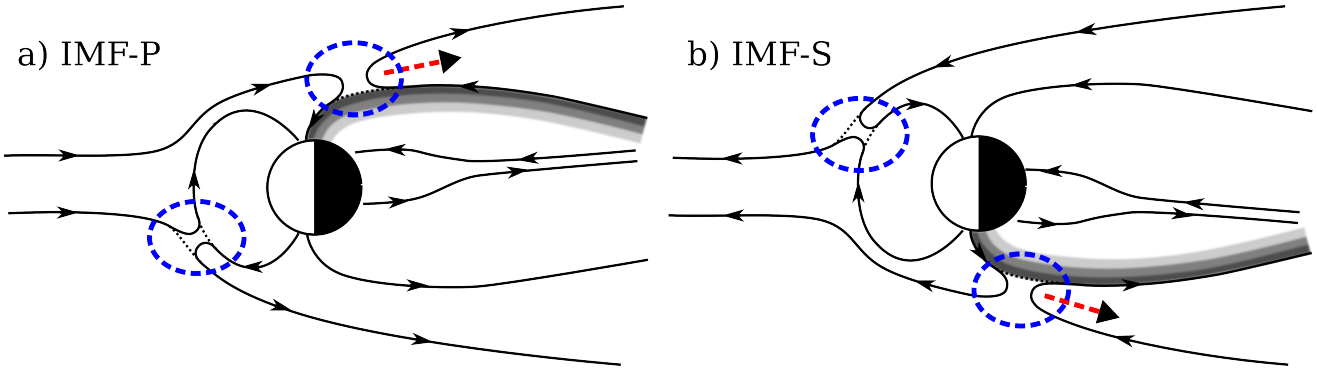

Figure 11. A sketch of the magnetospheric topology for the planetward (panel a) and the sunward (panel b) interplanetary magnetic field. The reconnection sites are indicated by the blue dashed ellipses. The red arrows indicate the magnetic curvature force direction. The shaded region shows the location of the plasma mantle.